IJCARS manuscript No.
(will be inserted by the editor)

3D Ultrasound Registration-based Visual Servoing for Neurosurgical Navigation

Oliver Zettinig[†] · **Benjamin Frisch**[†] · **Salvatore Virga** · **Marco Esposito** · **Anna Rienmüller** · **Bernhard Meyer** · **Christoph Hennersperger** · **Yu-Mi Ryang**[‡] · **Nassir Navab**[‡]

Received: Nov 04, 2016 / Accepted: Feb 01, 2017

Abstract *Purpose:* We present a fully image-based visual servoing framework for neurosurgical navigation and needle guidance. The proposed servo-control scheme allows for compensation of target anatomy movements, maintaining high navigational accuracy over time, and automatic needle guide alignment for accurate manual insertions.
Method: Our system comprises a motorized 3D ultrasound (US) transducer mounted on a robotic arm and equipped with a needle guide. It continuously registers US sweeps in real-time with a pre-interventional plan based on CT or MR images and annotations. While a visual control law maintains anatomy visibility and alignment of the needle guide, a force controller is employed for acoustic coupling and tissue pressure. We validate the servoing capabilities of our method on a geometric gel phantom and real human anatomy, and the needle targeting accuracy using CT images on a lumbar spine gel phantom under neurosurgery conditions.
Results: Despite the varying resolution of the acquired 3D sweeps, we achieved direction-independent positioning errors of 0.35 ± 0.19 mm and $0.61^\circ \pm 0.45^\circ$, respectively. Our method is capable of compensating movements of around 25 mm/s and works reliably on human anatomy with errors of 1.45 ± 0.78 mm. In all four manual insertions by an expert surgeon, a needle could be successfully inserted into the facet joint, with an estimated targeting accuracy of 1.33 ± 0.33 mm, su-

[†], [‡] These authors respectively contributed equally to this work.

Oliver Zettinig, Benjamin Frisch, Salvatore Virga, Marco Esposito, Christoph Hennersperger, Nassir Navab
Computer Aided Medical Procedures, Technische Universität München, Boltzmannstr. 3, 85748 Garching, Germany and Johns Hopkins University, 3400 North Charles Street, Baltimore, MD 21218, USA
Tel.: +49 89 289 17058, E-mail: oliver.zettinig@tum.de

Anna Rienmüller
Neurochirurgische Klinik und Poliklinik, Klinikum rechts der Isar, Technische Universität München, Germany and Department of Orthopedic Surgery, Medical University Vienna, General Hospital, Vienna, Austria

Bernhard Meyer, Yu-Mi Ryang
Neurochirurgische Klinik und Poliklinik, Klinikum rechts der Isar, Technische Universität München, Germany

perior to the gold standard.
Conclusion: The experiments demonstrated the feasibility of robotic ultrasound-based navigation and needle guidance for neurosurgical applications such as lumbar spine injections.

Keywords Registration-based Visual Servoing · 3D Ultrasound · Neurosurgical Navigation · Needle Insertion

1 Introduction

Due to its low cost, lack of ionizing radiation and ease of use, ultrasound (US) imaging is the modality of choice in a growing number of interventional scenarios. However, while its high spatial and temporal resolution are suited for real-time applications and movement-independent guidance, limited image quality and visibility of anatomy regularly limit its application in clinical routine. Therefore, the exclusive use of US imaging is not part of the standard of care for many interventions.

In this study, we focus on facet joint injections in the lumbar spine, which are either performed diagnostically to determine if the joint is a source of pain, or therapeutically for chronic spinal pain management [1]. In both cases, X-ray fluoroscopy guidance is recommended and considered gold standard [2]. Several studies have reported that US-guided injections show no significant difference in diagnostic accuracy and therapeutic efficacy compared to guidance using fluoroscopy or CT, yet substantially reduce the radiation exposure of both patient and clinicians [3–5]. Nevertheless, the limited field of view and difficulties in interpreting US images are common obstacles to guarantee accurate needle placement [2].

The manual navigation of the US transducer to the appropriate location and maintenance of a suitable acoustic window are linked to additional challenges. While the cumbersome procedure induces a slow learning curve [6,7], work-related musculoskeletal disorders have been associated with medical sonographers [8], impeding the quality of US-based interventions over time. Both of these issues relate to the freehand nature of previous US-guided facet joint injections, suggesting more automated solutions [9].

In this work, we propose a novel robotic visual servoing framework for neurosurgical navigation. Continuous re-registration of live 3D ultrasound images with an interventional plan, which is based on pre-interventional CT or MR images, allows for accurate guidance of manual needle insertions. Since the transformation obtained by the registration algorithm is directly fed to the robotic servo-controller, target anatomy movements are quickly compensated by re-adjusting the US transducer position. As a result, the presented system does not only relieve the physician from manually maneuvering the US probe while injecting the facet joint, but also provides continuous guidance regardless of target motion.

This study extends our previous, preliminary work [10] as follows:

i Several methodological improvements, including the performance of 3D ultrasound compounding and registration, enable real-time behavior of the system and greatly improve needle placement accuracy. In addition, a complete redesign of the transducer mount and needle holder now comply with clinical safety protocols.

ii Results of an extensive gel phantom analysis of the visual servoing system behavior are reported for target anatomy tracking under various conditions. By including smooth movements with different velocities and along different degrees of freedom, we estimate the limitations of the presented method.
iii A set of human volunteer experiments demonstrates the capabilities of the proposed visual servoing methodology under realistic conditions.
iv To demonstrate clinical feasibility, the proposed framework was validated within a realistic neurosurgical operating environment. We report first results of manual needle insertions performed by an expert surgeon into an ultrasound-realistic lumbar spine gel phantom and compare against the gold standard. For validation, a C-arm cone-beam CT system was used.

2 Related Work

Despite its disadvantages, ultrasound imaging has been successfully adapted for neurosurgical guidance. The simplest form of ultrasound-guided needle insertion is a visualization of the needle path, which is calibrated to a guide rigidly attached to the transducer, on the live 2D image [11, 12]. Since such approaches do not alleviate limited target visibility and poor contrast issues, optical or electromagnetic tracking systems were introduced, allowing for freehand 3D acquisitions that can be registered to pre-operative imaging data such as CT [13,14]. Assuming that the patient has not moved, features such as vertebrae contours can be then highlighted on the live US image along with the insertion path of a tool, which is also coupled with a tracking target. When pre-interventional images are not available, registration can also be established with statistical spine atlases, which have been shown to provide enough context for successful needle insertions [15]. A further extension superseded the need for a tracking system by falling back to an attached needle guide and employing a motorized transducer, directly enabling 3D US acquisition [12]. In return for a greatly reduced frame rate on the insertion plane, this system provides updated anatomy highlighting also if either transducer or patient move. However, none of the aforementioned works eliminate the need for manually maintaining sufficient image quality with the handheld US probe.

To overcome this limitation, robotic assistance in combination with visual servoing techniques has been studied in previous works. By extracting features from live 2D or 3D images, tracking of various anatomies such as the carotid artery as well as of surgical tools has been achieved based on ultrasound [16, 17]. When coupled with a robot control scheme, applications such as organ motion compensation [18] and visibility maintenance in tele-operation [19] become feasible. More advanced image processing, including the computation of confidence maps, recently enabled more reliable automated maintenance of US quality [20], which was applied to abdominal aortic aneurysm screening [21].

Using static transducers, ultrasound servoing has in prior art mostly been employed for needle tracking and robotic steering [22, 23]. Because the developed control schemes can broadly be translated to robotically steered US probes, a full automation of dedicated parts of surgeries comes into reach, for instance by simultaneous tracking of both anatomy and instruments [24]. Yet, complete image-based 3D-to-3D volume registration for the purpose of US transducer visual servoing has,

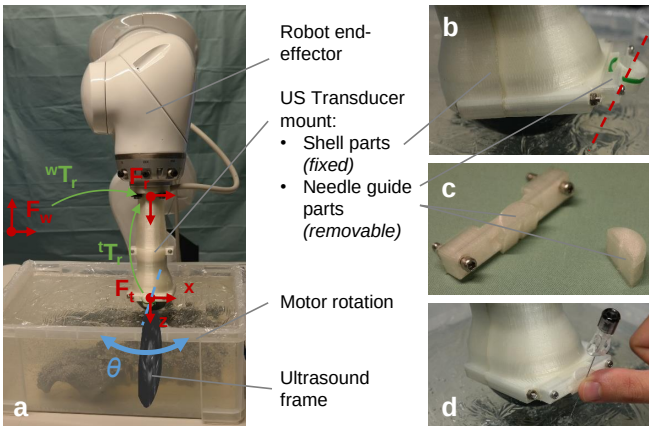

Fig. 1: **a)** System design including robot, mount, motorized US transducer (θ denotes the motor angle) and needle guide. The green transformations map between world (F_w), robot end-effector (F_r) and US transducer (F_t) coordinate frames. **b-c)** The mount consists of four parts: Two fixed shell parts and two removable needle guide parts. **d)** When the outer needle guide shell is removed, accurate and safe guidance is possible using a finger.

to the best of our knowledge, not been achieved apart from our preliminary results in [10].

3 Methods

The proposed neurosurgical navigation framework uses a robotic manipulator, to whose end-effector a motorized ultrasound transducer is rigidly attached (see Fig. 1a). Before detailing the robot control laws, we describe how visual servoing-based neuronavigation can be employed in clinical workflows.

3.1 Neurosurgery Workflow

In Fig. 2, an exemplary clinical workflow for lumbar facet joint needle insertions is depicted. Adequate imaging of the patient is required for manual path planning (I_p). Ideally, pre-interventional CT (as in the figure) or MR images are available, which is commonly (but not necessarily) the case in today's practice to confirm the treatment indication. Yet, 3D ultrasound volumes as acquired during the robotic sweep would be sufficient as long as the joints can be clearly visualized. Along with the needle path, annotations such as vertebrae labels can be added.

Once the patient is positioned in the intervention room and sufficient ultrasound gel is applied, the robot can be manually steered towards the patient's sacrum in gravity compensation mode. It will then automatically approach the skin until a predefined scanning force is reached, and automatically perform an initial US sweep in caudocranial direction. The sweep is compounded to a 3D image I_0 and registered to the pre-interventional image I_p.

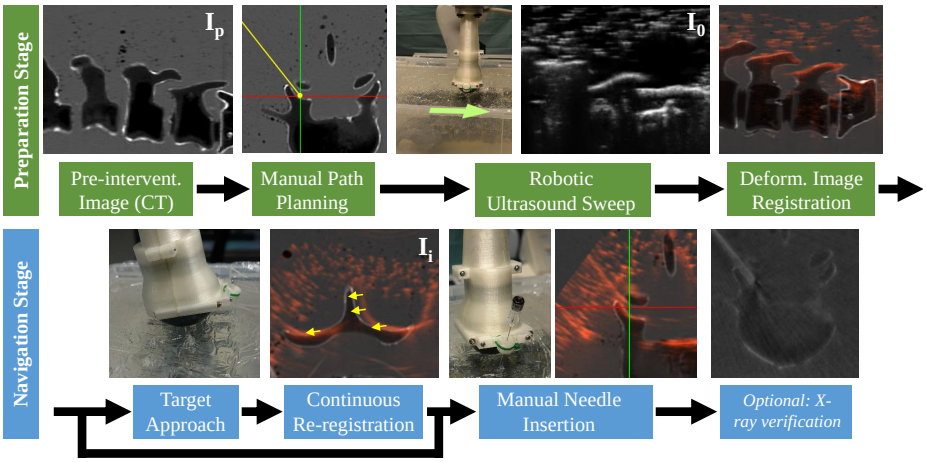

Fig. 2: Workflow for facet joint needle insertion using the proposed ultrasound-based visual servoing guidance framework. In the **preparation stage** (*green*), a multi-modal set of images is acquired and registered to establish an interventional plan in the current patient coordinate system. Thereafter, the automatic navigation system takes over during the **navigation stage** (*blue*), maintaining registration over time and enabling precise manual needle insertion.

At this point, the system is prepared to start the navigation stage and approach the target position by aligning the needle guide attached to the US transducer (see Fig. 1b) with the planned needle path. The proposed visual servoing scheme performs a continuous re-registration of the target region in 3D and compensates for patient motion (note that the patient is awake throughout the entire intervention). Eventually, the surgeon manually inserts the needle under ultrasonic guidance. If desired, a multi-planar reconstruction of the registered pre-interventional image can be visualized for better contrast. As a final step, since the needle guide can be opened and the robot manually removed at any time, traditional X-ray verification of the final needle position is easily possible before drug injection. Note that this optional step is intended for clinical verification studies but not the final, radiation-free interventional procedure.

3.2 Control Architecture

Two distinct control laws are jointly responsible for robot movements, as illustrated in the control fusion architecture in Fig. 3. On the one hand, a compliant direct force controller maintains a constant contact force onto the patient, ensuring sufficient image quality yet allowing the patient or operator to manually move the robotic arm away, if it were needed. On the other hand, the objective of the visual control law is to update the desired pose of the US transducer by means of 3D image registration. This allows to follow and compensate for target anatomy movements, and to keep the needle guide aligned with a pre-interventional plan. In the subsequent sections, the necessary control laws to achieve these goals are explained.

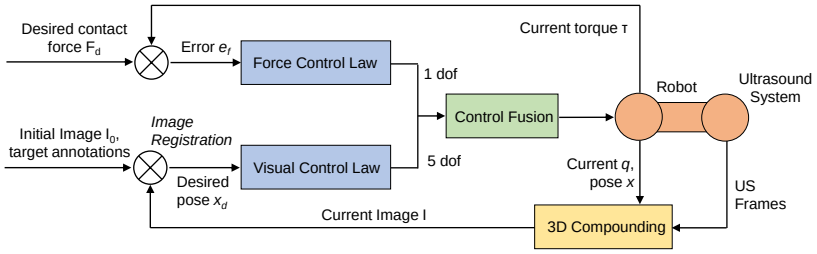

Fig. 3: The dual control architecture combines force control with visual servoing in a parallel fashion.

3.3 Force Control Scheme

For optimal ultrasonic acquisitions, a constant contact force onto the surface is desirable. A compliance control scheme is adopted to regulate the robotic manipulator, which allows to relate the displacement of the end-effector to the forces acting on it. Considering the tool center point (TCP) frame of the end-effector, it is possible to control the force applied along a constrained task direction, while the position of the end-effector is controlled along the unconstrained task directions. In our setup, the constrained direction is the z-axis of frame F_t, which is the orthogonal vector to the contact surface. For a manipulator with compliant joints and rigid links, the generalized end-effector stiffness matrix $\mathrm{K}_{TCP} \in \mathbb{R}^{m \times m}$ can be expressed in task space as in [25]

$$F_{TCP} = \mathrm{K}_{TCP}\,(x - x_0) = \mathrm{K}_{TCP}\,\Delta x, \tag{1}$$

where $F_{TCP} \in \mathbb{R}^m$ is the external force at the robot end-effector, x_0 and $x \in \mathbb{R}^m$ are the initial and the current Cartesian position of the robot, respectively, and $\Delta x \in \mathbb{R}^m$ is the position displacement. For planar contact surfaces, a constant force along the constrained direction is obtained with the selection of the desired force F_d and a low stiffness K_d as values of the respective components along the constrained axis in F_{TCP} and K_{TCP}. A high stiffness along the remaining components allows for a classic position control schema in the other directions. That is, while the given desired force F_d and stiffness K_d determine the end-effector position along its z-axis, the remaining degrees of freedom can be controlled by the proposed visual control scheme, as shown in Fig.3. Due to the compliance of the system, the robot can be manually moved away from the contact surface at any time, either by the patient or the physician. During needle insertion, this is useful to make slight adjustments, if necessary.

3.4 3D Ultrasound Image Acquisition and Preparation

In this work, 3D ultrasound volumes are used for all visual servoing purposes. To this end, individual 2D B-mode frames are compounded using a GPU-based backward warping strategy as in [26]. For every single frame, the full chain of transformations into the world coordinate frame F_w is considered (see Fig. 1a):

$${}^{us}\mathrm{T}_w = ({}^{w}\mathrm{T}_r)^{-1} \cdot {}^{t}\mathrm{T}_r \cdot \mathrm{T}_\theta \cdot \mathrm{Z}, \tag{2}$$

where Z is the intrinsic calibration determined using the known pixel spacing and the pixel coordinates of the first center US ray sample as provided by the US system, and T_θ a rotation matrix determined by the current motor position θ of the US transducer. The extrinsic calibration ${}^{t}\mathrm{T}_r$ is initialized based on the CAD design of the mount and fine-tuned using orthogonal robotic sweeps similar to [27]. Finally, ${}^{w}\mathrm{T}_r$ is the current end-effector pose of the robot. Note that as the 3D compounding is performed in world space F_w, this allows for undistorted 3D volumes even if the robot is moving during acquisition, in contrast to only ultimately placing the already compounded sweep into the world frame as in [10].

During the acquisition of the initial sweep (I_0), the motor of the transducer is turned off ($\theta = 0$) so that parallel frames are acquired. A deformable registration to the pre-interventional image I_p is performed by estimating a non-linear transformation $\tilde{T}_p$:

$$\tilde{T}_p = \arg\max_T S_{LC^2}(\mathrm{I}_0, T(\mathrm{I}_p)), \tag{3}$$

where S_{LC^2} is the multi-modal LC^2 similarity metric [28], efficiently evaluated on the GPU. The transformation T is modeled using free-form deformations [29]. Its semi-automatic initialization is facilitated by the assumption that the robotic scan starts at the sacrum and continues in cranial direction, resolving the rotatory alignment of I_0 and I_p. As a result, the inferior-superior axes can be roughly aligned automatically, only necessitating a quick manual translation to complete the initialization. Due to the visibility of the sacrum, a reliable mapping of vertebrae is easily possible, helping to avoid level misalignments. All manual annotations can be embedded in the world coordinate frame F_w using the final transformation $\tilde{T}_p$, including the planned needle path. The optimization of the parameters is performed using BOBYQA [30].

For continuous re-registration, sweeps to acquire images I_i are obtained using the transducer motor. Only in the final stage during manual needle insertion, the motor is turned off again to enable high frame rate visual 2D feedback to the surgeon. The lack of 3D imaging information then also prohibits further automatic robot pose updates, avoiding harm to the patient once the needle has been inserted.

3.5 Visual Control Scheme

The visual servoing controller is based on our previous work [10], where instead of defining and optimizing some visual error functional, a transformation $\hat{T}_i$ to align two 3D ultrasound images is directly estimated using registration and then used to update the desired robot pose[1]:

$$\hat{\mathrm{T}}_i = \begin{pmatrix} \mathrm{R}(\alpha,\beta,\gamma) & (t_x, t_y, t_z)^\intercal \\ 0 & 1 \end{pmatrix} = \arg\max_T S_{NCC}(\mathrm{I}_i, T(\mathrm{I}_0)). \tag{4}$$

In this work, we assume locally rigid movements [31], constituting six degrees of freedom. R denotes a 3×3 rotation matrix parametrized with Euler angles α, β, γ. The fixed image is now the most recent 3D compounding I_i, and the moving one the initial US sweep I_0 with all annotations. Normalized cross correlation

[1] Throughout this article, linear transformations and vectors are expressed in computer vision notation, i.e. using 4×4 homogeneous matrices and 4×1 vectors.

(NCC) is employed for the similarity S_{NCC}, as both volumes are derived from the same modality [31]. The transformation is initialized with the previous registration result for fast convergence. In addition, the degrees of freedom of the optimization procedure are restrained, since pose updates in the direction of the z-axis of frame F_t will be ignored anyway by the force controller. The exclusion of further degrees of freedom is also possible, e.g. if only translations are expected.

If there has been no change of the target anatomy, both images will be almost identical, and the similarity function S_n at a local maximum with all transformation parameters set to 0. Small movements, however, can be recovered efficiently within a few iterations of the optimizer, directly allowing for their compensation with the obtained transformation $\hat{\mathrm{T}}_i$.

In scenarios without a needle guide, where the system is purely used to track a moving target, the visual control law determining a new, desired Cartesian pose of the US transducer is formulated as follows:

$$x_{d_i} = ({}^{t}\mathrm{T}_r)^{-1} \cdot (\hat{\mathrm{T}}_i)^{-1} \cdot \mathrm{P}_0, \tag{5}$$

where P_0 is a manually annotated US transducer target pose defined either directly in the initial sweep I_0 or transformed from the pre-interventional image: $\mathrm{P}_0 = \tilde{T}_p(\mathrm{P}_p)$.

If a needle guide needs to be aligned with a predefined insertion path, additional constraints based on two further manual annotations have to be considered. Let t_0 be a needle target point and $\overrightarrow{s_0}$ a suitable insertion path, both defined in I_0 similarly to P_0. Furthermore, consider a set of two points in transducer frame F_t, m_0 and n_0, to indicate two points the needle would hit if inserted into the guide. Obtained once by calibration in water using manual annotation of two arbitrary needle points, they can be expressed in the world frame using the known chain of transformations. All are carried along in each iteration as the target might have moved:

$$\left[t_i \ \overrightarrow{s_i}\right] = (\hat{\mathrm{T}}_i)^{-1} \cdot \left[t_0 \ \overrightarrow{s_0}\right], \tag{6}$$

$$\left[m_i \ n_i\right] = (\hat{\mathrm{T}}_i)^{-1} \cdot ({}^{w}\mathrm{T}_r)^{-1} \cdot \ {}^{t}\mathrm{T}_r \cdot \left[m_0 \ n_0\right]. \tag{7}$$

The normalized needle guide direction can then be defined as $\overrightarrow{l_i} = (m_i - n_i)/\left\|m_i - n_i\right\|$ [10]. The required correction to orient skew $\overrightarrow{s_i}$ and $\overrightarrow{l_i}$ in a parallel fashion is a rotation

$$\mathrm{C}_i = \mathrm{R}(\overrightarrow{s_i} \times \overrightarrow{l_i}, \mathrm{acos}\langle\overrightarrow{s_i}, \overrightarrow{l_i}\rangle), \tag{8}$$

where R converts the axis-angle representation to a 3×3 matrix. An additional offset is finally necessary to let both lines coincide:

$$\overrightarrow{u_i} = (m_i - t_i) - \overrightarrow{s_i} \cdot \langle\overrightarrow{s_i}, m_i - t_i\rangle \tag{9}$$

Together, these two adjustments are embedded into the matrix

$$\mathrm{H}_i = \begin{pmatrix} \mathrm{C}_i & \overrightarrow{u_i} \\ 0 & 1 \end{pmatrix}, \tag{10}$$

which forms the basis for the modified visual control law

$$x_{d_i} = ({}^{t}\mathrm{T}_r)^{-1} \cdot \mathrm{H}_i \cdot (\hat{\mathrm{T}}_i)^{-1} \cdot \mathrm{P}_0. \tag{11}$$

4 Experiments

4.1 System Setup

As shown in Fig. 1a, a KUKA® LBR iiwa 7 R800 robot (KUKA Roboter GmbH, Augsburg, Germany) is employed for all experiments. The manipulator is equipped with torque sensors in all joints, allowing for impedance control applications. A KUKA Sunrise Connectivity SmartServo application[2] is utilized to connect to ROS (Robot Operating System[3]) on a client workstation for reporting the current robot status with 400 Hz, including the current end-effector pose ${}^{w}\mathrm{T}_{r}$, and executing incoming commands [21]. The robot is certified for human interaction and can be safely used in collaborative scenarios. Desired force and stiffness in tool direction were set to $F_d = 5$ N and $K_d = 0$ N/m, respectively. The stiffness in all other directions was fixed to $1,000$ N/m.

An Ultrasonix® Sonix RP system with a motorized curvilinear transducer (model 4DC7-3/40 Convex 4D) is used for B-mode acquisition (BK Ultrasound, Analogic Corp., Peabody, MA, USA). The 2D acquisition rate of the curvilinear array was set to 30 Hz. The motor speed was defined so that sweeps of $\pm 15°$ are covered at 4 Hz. The frequency, depth and gain were set to 3.3 MHz, 70 mm, and 50%, respectively. A modified component in the publicly available PLUS library 2.2.0 [32], based on the Ultrasonix Porta SDK 5.75, maintains a bi-directional OpenIGTLink [33] Ethernet connection to the client workstation for a) streaming incoming B-mode frames and b) receiving user commands to start and stop the motor as desired.

A custom 3D-printed mount consisting of four parts is used to attach the US probe with the manipulator and allows for needle guidance, as shown in Fig. 1b. It is designed to meet the safety and hygienic requirements of clinical environments. Two symmetric shell parts surround the transducer and enable the fixation to the end-effector using four screws, forming a permanent fixation of the two devices to avoid frequent calibration procedures. In contrast, a semicircular needle guide with desired inclination can be individually attached for an intervention (see Fig. 1c-d). Its open design allows an operator to guide the needle by hand but remove the compliant robot at any time, even after the needle is already partially inserted. Finally, an optional second semicircular shell makes it possible to completely surround the needle for highest precision guidance. All parts in contact with the needle are quickly removable and can be manufactured either for single-use or for re-use after sterilization.

The essential part of the proposed visual servoing control scheme is the image processing component, for which a set of custom plugins for ImFusion Suite 1.2.43 (ImFusion GmbH, Munich, Germany), an extensible GPU-based framework for medical images, is used. Running on the mentioned client workstation (Intel® Core i7-4770K processor at 3.5 GHz, 32 GB RAM, NVIDIA® GeForce GTX 770 graphics card), they incorporate OpenIGTLink and ROS interfaces and implement the visual control laws described in the methods section. After the acquisition of each US sweep (4 Hz), 3D compounding on the GPU to volumes with an isometric resolution of 0.3 mm adds latency of around 30 ms. Compounding

[2] `https://github.com/SalvoVirga/iiwa_stack`

[3] `http://www.ros.org/`

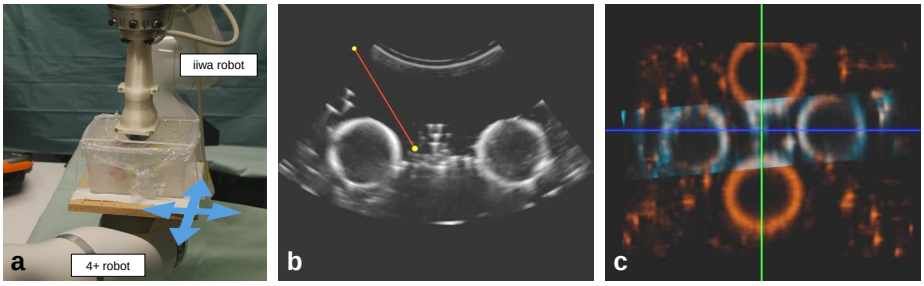

Fig. 4: **a)** Experimental setup for servoing validation experiments. A second robot holds a geometrical gel phantom and moves horizontally. **b)** Center US frame and **c)** coronal slice of the compounded 3D US volume. In the latter, the *blue* volume is the current volume, and the *red* one the initial sweep the algorithm continuously registers against.

tasks run in parallel to the continuous registration tasks, which also utilizes the graphics processor for the evaluation of the NCC similarity metric. The registration is performed with a fixed time budget of 230 ms, and the result is discarded if the optimizer has not converged until then.

4.2 Experimental Phantoms

Phantoms were specifically created for all conducted experiments, offering realistic contrast in both ultrasound and CT. As tissue mimicking material, Ceraflex N530 transparent gel (Th. C. Tromm GmbH, Cologne, Germany) was used. Lab experiments to validate the visual servoing control schemes were performed on a geometric phantom consisting of 4 rubber spheres (diameters 2× 27 mm, 2× 35 mm) embedded in a 180×160×90 mm box filled with gel (see Fig. 4).

For needle insertions experiments, a realistic and radiopaque spine phantom was made. A lumbar spine model (vertebra L1 to sacrum; Sawbones, Pacific Research Laboratories Inc., Vashon Island, WA, USA) was embedded in a gelatinous box, approximately the size of an adult human abdomen (380×240×150 mm). To avoid an unrealistically homogeneous gel filling, the gel was poured quickly and cooled to 5 °C immediately after. This allowed for the retention of air bubbles, generating challenging speckle noise in the US images.

4.3 Visual Servoing Performance on Phantom and Human

In order to evaluate the tracking and motion compensation capabilities of our system, the geometric phantom was attached to a second robot, KUKA LWR 4+ (KUKA Roboter GmbH, Augsburg, Germany), as shown in Fig. 4a. After manual positioning of the ultrasound equipped robot such that the central ultrasound frame roughly contained both smaller spheres' centers, a horizontal sweep of ±60 mm was acquired for subsequent registration (Fig. 4c, *red* volume).

Three sets of experiments were conducted to measure the influence of various parameters on the tracking performance. At each point in time t, the spatial lag $\Delta s(t) = \|\Delta p_{iiwa} - \Delta p_{4+}\|$ is measured as the difference between the relative movements of both robots. Depending on the experiment, $\Delta p = p(t) - p(t_0)$ either extracts the translation on the horizontal plane ($p_t = [t_x\ t_y]^\intercal$) or the rotation around the z-axis ($p_\gamma = [\gamma]$) of the end-effector poses, which were recorded at 50 Hz. In addition to the initial temporal lag Δt_0, i.e. the time between the onset of both robots' movements, we defined the time until convergence Δt_c as the time from the end of the 4+ movement until $t_e : \Delta s(t) < 0.05$ mm $\forall t > t_e$. The final positioning error after convergence was then defined as $e_p = \Delta s(t_e)$. Because only such relative movements were considered and the robots were aligned by design, we abstained from performing an additional robot-to-robot calibration.

In the first set of experiments (A), the lower robot was smoothly moved orthogonally to the central US image plane, i.e. along the x-axis of F_t, with different velocities v between 12 and 32 mm/s by 280 mm. The degrees of freedom for the registration were restricted to t_x and t_y to avoid that the registration exceeded its time budget. In the second set of experiments (B), the phantom was rotated by 45° with different angular velocities ω between 3.6 and 14.3°/s. In a last set of experiments (C), the phantom was translated with constant, intermediate velocity of $v = 15$ mm/s in different directions ϕ by 150 mm to estimate whether motions orthogonal to the central US frame yield higher errors than the ones parallel to it. Finally, we performed a drift experiment over a time span of 4 minutes with several translations within a 200×100 mm box with $v = 12.1$ mm/s.

In a similar manner, the tracking performance was validated on the real anatomy of a human volunteer (male, age 28). As shown in Fig. 8a, the subject was positioned in prone position on a wheeled bed, steerable in all directions, and instructed to perform regular, shallow breathing. Instead of a second robot performing translations, the bed was manually moved with 5-10 mm/s perpendicular and orthogonal to the central US frame. An NDI® Polaris Vicra (Northern Digital Inc., Waterloo, ON, Canada) was used to measure ground truth positions. The tracking target was fixed to the subject, as close as possible to the lumbar spine. A hand-eye calibration as in [34] was performed to facilitate reporting of the spatial lag on the horizontal plane, analogously defined as $\Delta s(t) = \|\Delta p_{iiwa} - \Delta p_{NDI}\|$, and the resulting positioning error e_p, where p_{NDI} denotes the position of the tracking target in frame F_w.

4.4 Needle Insertion Accuracy

To validate the navigation capabilities of the proposed framework, needle insertion experiments were conducted in a realistic neurosurgical operating environment by two expert spine surgeons with standard 22G needles of 88 mm length. The phantom was positioned on an operating table in prone position as shown in Fig. 5a. The workflow as described in the methods section was fully carried out four times, each starting with a manual path annotation by one surgeon in a preoperatively acquired navigation CT image, as illustrated in Fig. 5b (*bottom*). After robotic target approach and registration-based refinement, four needles were inserted under live US guidance by the same surgeon who annotated the plan. For

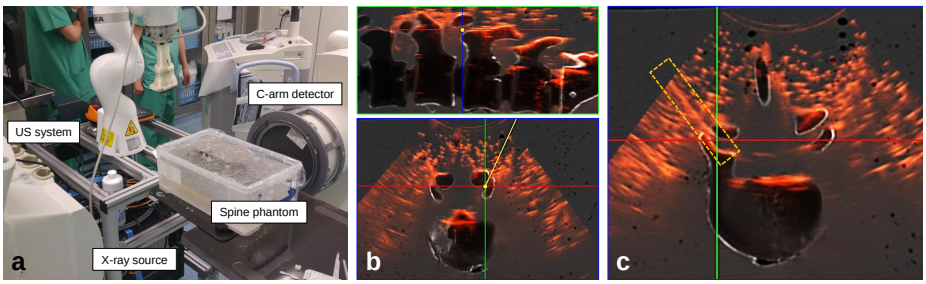

Fig. 5: **a)** Experimental setup in neurosurgery OR. **b)** Planned needle path shown in sagittal (*top*) and axial (*bottom*) slices of pre-interventional CT (*grayscale*) registered to initial US sweep (*red*). **c)** Needle can be clearly visualized in US during and after insertion (*yellow box*).

the first two, the closed needle guide (Fig. 1b) was used, for the last two, the open one in combination with a finger as depicted in Fig. 1d.

To compare with the gold standard, four additional needles were inserted by a surgeon without robotic assistance but under X-ray fluoroscopy guidance, for which a Siemens Arcadis® Orbic 3D iso-C-Arm system (Siemens Healthineers GmbH, Erlangen, Germany) was used. The C-arm was also used to acquire 3D fluoroscopy scans (CBCT), as shown in Fig. 9, to allow quantification of the achieved placement accuracies in both cases.

Two error measures were used. First, the total Euclidean error $e_d = \|t_0 - t_v\|$ reports the distance between the planned needle target t_0 and the manually annotated tip of the needle in the CBCT image, denoted t_v and reported in frame I_0 after registration to the already deformed ($\tilde{T}_p$) pre-interventional image. Second, since the presented navigation system has no influence on the manual insertion depth, the orthogonal error $e_\perp = \|t_0 - t_v - \langle \overrightarrow{s_0}, t_0 - t_v \rangle\|$ reports the perpendicular component of e_d, i.e. the distance of the needle tip to the planned insertion line.

5 Results

5.1 Visual Servoing Performance

Table 1 lists mean and standard deviation for the mentioned metrics for all experiments. For easy comparison, positions of both robots during all experiments of set A are collectively visualized in Fig. 6a. Only for the fastest motion with $v = 32$ mm/s, tracking was lost. In all other cases, the continuous movements were reliably detected and compensated by the visual servoing controller. As shown in Fig. 6c (*red curve*), we found a strong linear correlation between v and the average lag $\Delta\overline{s}$ ($R^2 = 0.98$), which is shown in Fig. 6b. Below the limit of the US resolution in transducer sweep direction (ca. 1 mm at the depth of the spheres), the final error e_p increased approximately in a linear fashion with higher velocities (overall $R^2 = 0.82$, see Fig. 6b, *blue curve*). Similar results were obtained for the experiment set B, with no clear relation between ω and error e_p. For experiments C,

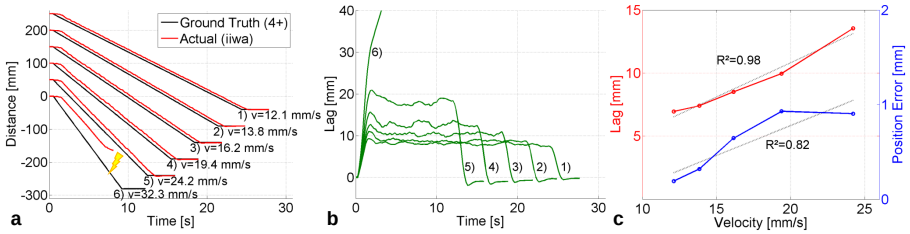

Fig. 6: Experiments *A*. **a-b)** Tracking was successful in all experiments except the one with fastest motion (32 mm/s), with spatial lags of less than 20 mm, almost no overshoot and fast convergence. **c)** Strong linear relation between the velocity and the spatial lag (*red, left ordinate*) as well as final position error (*blue, right ordinate*).

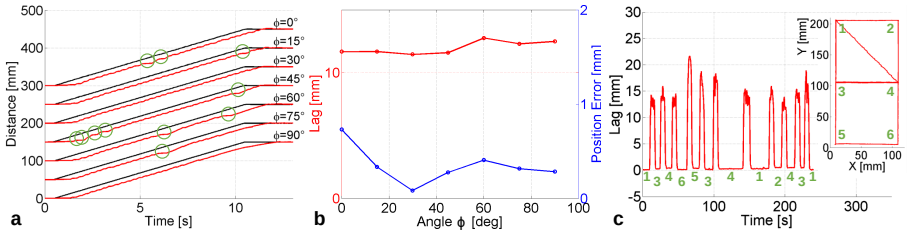

Fig. 7: **a)** Experiments *C*. Trajectories of both robots show successful tracking in all experiments even though the continuous registration occasionally exceeded its time budget (*circles*); **b)** both the spatial lag (*red, left ordinate*) and the final position error (*blue, right ordinate*) were independent of the translation angle ϕ. **c)** Spatial lag during several consecutive translations between corner points (labeled in *green*) of the box shown in the inlet suggests the absence of a drift over time.

the positions of both robots during all experiments, projected into the respective vertical plane, are collectively visualized in Fig. 7a. The registration exceeded its time budget 11 times (≈3.3%), not updating the desired robot pose, (*see green circles*) but recovered quickly in all cases. No clear relation between ϕ and $\Delta\bar{s}$ (see Fig. 7b, *red curve*) was found. The positioning error e_p was also independent of ϕ (see Fig. 7b, *blue curve*), as long as the movement was not exclusively orthogonal to the central US plane (highest error $e_p = 0.73$ mm for $\phi = 0$). In all 17 experiments (*A*-*C*), we found Δt_0 and Δt_c to be independent of the examined parameters. In both cases, the random time until the completion of the next US sweep due to the significantly lower update rate compared to the robot was the determining factor. Finally, as depicted in Fig. 7c, the robot returned in the drift experiment to its initial position after 11 translations with an error of $e_p = 0.05$ mm, suggesting the absence of any drift over time. The average spatial lag after convergence of each section was 0.26 ± 0.15 mm.

The tracking performance for the human subject experiment is visualized in Fig. 8b, first showing translations perpendicular to the central US plane (*top*), followed by ones parallel to it (*bottom*). The spatial lag $\Delta\bar{s}$ during movements was on average slightly lower for the former (8.26 vs. 9.32 mm). In total, 11 translati-

Table 1: Results of the three sets of visual servoing experiments, reporting the number of experiments per set N, average spatial lag $\Delta\bar{s}$, time until initial movement Δt_0, time until convergence Δt_c and the final positioning error e_p.

Set	Param.	N	$\Delta\bar{s}$	Δt_0 [s]	Δt_c [s]	e_p
A: Translation	v	6	9.27 ± 2.65 mm	0.46 ± 0.18	0.96 ± 0.18	0.59 ± 0.33 mm
B: Rotation	ω	4	$5.85° \pm 4.2°$	1.05 ± 0.14	1.36 ± 0.43	$0.61° \pm 0.45°$
C: Translation	ϕ	7	12.00 ± 0.51 mm	0.70 ± 0.11	1.16 ± 0.25	0.35 ± 0.19 mm

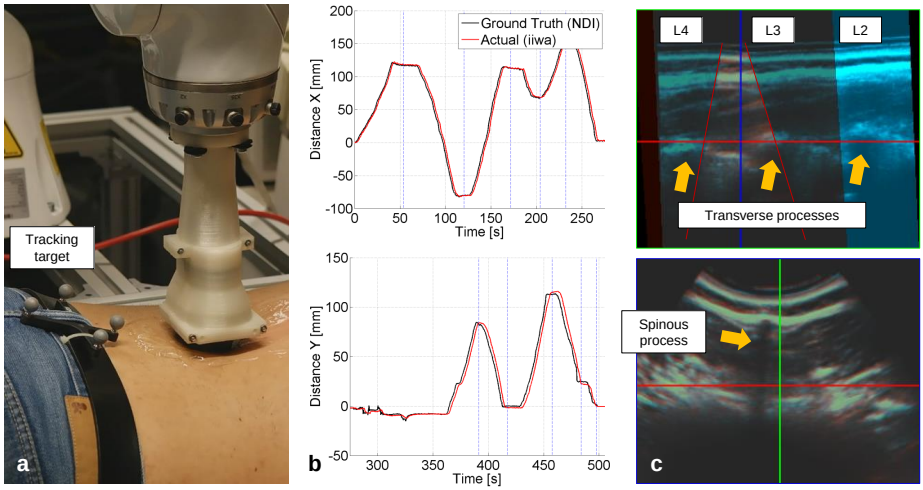

Fig. 8: **a)** Experimental setup for human volunteer experiments with optical tracking target. **b)** Trajectories of robot and body tracking target over 500 seconds, showing excellent visual servoing behavior. Translations along the x- and y-axes of F_t were performed consecutively. **c)** Exemplary initial US sweep (*blue*) with overlay of one motorized sweep after registration (*red*). Anatomical landmarks annotated for reference.

ons were performed. The positioning error e_p after convergence of each segment, indicated as blue lines in Fig. 8b, was on average 1.45 ± 0.78 mm. The maximum error was 2.72 mm. Exemplary US images are shown in Fig. 8c, including both an initial sweep (*blue*) and one motorized sweep (*red*). Several anatomical structures as inherently used for alignment during continuous re-registration are highlighted for better understanding. As long as the subject maintained low tidal volumes, no detrimental respiratory disturbances in the horizontal plane were encountered. Similar to [35], maximum displacements in vertical direction were around 2 mm.

5.2 Needle Insertion Accuracy

All eight insertions into the facet joint were deemed technically successful by the expert spine surgeon (needle tip in the gap between the articular processes [7]), with average orthogonal positioning errors for robotic and conventional way of

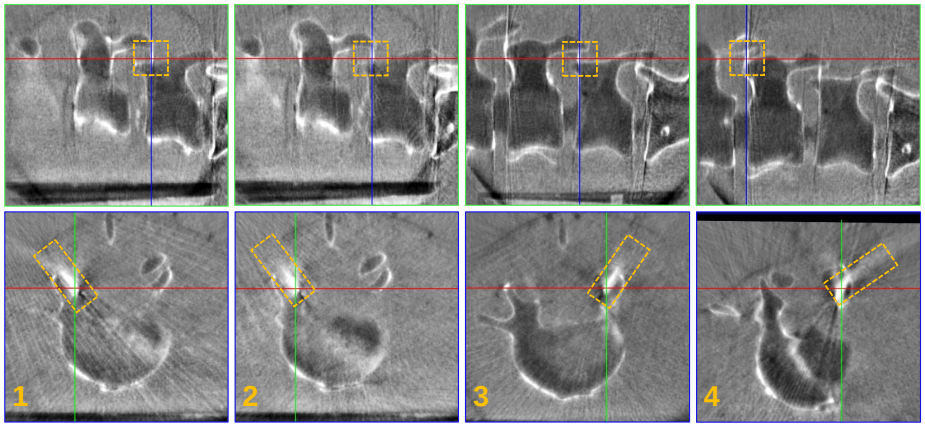

Fig. 9: Sagittal (*top*) and axial (*bottom*) slices of the verification cone-beam CT images after robot assisted needle insertion, showing successful targeting of the facet joint in all cases (*yellow boxes*).

Table 2: Results of the needle insertion experiments, comparing accuracies achieved with and without robotic assistance.

Needle	Robotic Assistance (Ultrasound)				Conventional (X-ray)		
	Site	Guide	e_d [mm]	$e_\perp$ [mm]	Site	e_d [mm]	$e_\perp$ [mm]
1	L4-5 R	closed	1.57	1.55	L4-5 R	4.29	3.22
2	L4-5 R	closed	1.46	1.20	L3-4 R	3.96	2.89
3	L4-5 L	open	1.83	1.71	L4-5 L	1.28	1.27
4	L3-4 L	open	3.60	0.97	L3-4 L	1.93	1.34
Avg.			2.12 ± 1.00	1.36 ± 0.33		2.86 ± 1.49	2.18 ± 1.02

guidance of 1.36 ± 0.33 mm and 2.18 ± 1.02 mm, respectively. All results are reported in Tab. 2, and CT slices of the phantom after robot assisted insertions in Fig. 9. An exemplary registration result between pre-interventional CT and the initial US sweep I_0 is visible in Fig. 5b. Figure 5c shows an exemplary live US guidance view, which was used by the expert neurosurgeon to insert the needle. The average time from manual path planning to manual needle tip annotation in the CBCT image was 25 min for the robotic case, with routine established quickly so that the last iteration only took 11 minutes. As the conventional needle insertions were performed by an expert, the total applied X-ray dosage for navigation only amounted to 5.93 cGycm^2. For each of the CBCT acquisitions, 15.11 cGycm^2 were measured (rotation by 190° while acquiring 100 images in 60 seconds).

6 Discussion

In this work, we have presented a complete ultrasound-based visual servoing framework dedicated to neurosurgical navigation. Continuous real-time re-registration

allows for the compensation of target motion and the precise alignment of a needle guide according to a pre-interventional plan.

The phantom experiments indicated that visual servoing-based tracking of moving anatomies is possible with velocities of up to 25 mm/s. This should exceed the expected velocities in neurosurgical scenarios, which are dominated by respiratory movements [35]. In combination with the spatial lag achievable by the system, higher velocities would lead to the target leaving the capture range of the similarity metric [28] or the field of view of the US transducer completely. The obtained results thus do not only show that tracking with submillimeter accuracy is possible as long as sufficient 3D image contrast is available to guide the image registration, but also that there is no drift over time. Both characteristics of the presented system are evenly important for interventions necessitating image guidance over longer time spans. Despite the smaller field of view and the higher 3D ultrasound frame rate, in turn reducing the spatial resolution in sweep direction, overall smoother movements than in [10] with an oscillation-free convergence behavior (no overshoots) have been achieved due to the improved 3D compounding methodology. As a result, the average time until convergence could be reduced to a clinically acceptable level.

Similar to the phantom experiments, the system was also able to successfully track human vertebrae under realistic conditions in volunteer experiments. Movements orthogonal to the central US frame were slightly lower than when the subject moved parallel to it. This is counterintuitive due to the lower resolution in this direction, and can possibly be explained by the better coverage with the initial sweep. Although the final positioning errors were higher than in phantom experiments, the achieved accuracy is well below the size of the target anatomy for facet joint injections [36].

Although the registration optimizer occasionally exceeded its fixed time budget, any temporarily increased spatial lag could be reliably compensated, yielding successful tracking outcomes in all experiments. Nevertheless, the issue could potentially be resolved by using the optimal transformation parameters at the end of the allotted time slot as initialization for the subsequent registration task. A Kalman filter [37] could furthermore improve the lag of the system and help avoiding the propagation of wrong local minima captures. In addition, the application of motion prediction algorithms as in [38] might be a starting point to better cope with repetitive motions such as breathing with higher amplitude than in the conducted experiments, which was not investigated in this work.

One major limiting factor of the presented system is the update rate of the motorized US transducer. While the usage of 4D matrix probes or very high frame rate technology [39] will be suited to improve the rate at which 3D volumes can be acquired, the bottleneck of 3D image registration will remain, in particular if many degrees of freedom are considered for optimization. Adaptive strategies to for example reduce the image size (downsampling) during rapid movements until target approach might mitigate this limitation in future studies.

Promising needle placement results were obtained in the spine phantom experiments using the proposed needle guidance system. For the first time, a robotic ultrasound-based navigation system has been employed to allow manual needle insertions into the narrow facet joint with clinically sufficient accuracy [36], which has been significantly improved compared to [10]. No differences in needle placement accuracy could be identified concerning the type of needle guide (open vs.

closed). In comparison to the proposed system, our X-ray guidance experiments demonstrated the placement variability of the conventional approach. Yet, the obtained errors should be interpreted with care, as the planned target positions were chosen to be further within the facet joint for better US-guided aiming, while the conventionally inserted needles approached the joints in a slightly steeper angle. The experimental setup in a realistic neurosurgical environment proved the clinical applicability of the system. In particular, the sharp decrease in procedure time throughout the conducted experiments underlined its minimal overhead and usability without extensive training. The compatibility with existing C-arm systems in terms of space and workflow requirements directly open the possibility of a subsequent clinical study, comparing the accuracy, efficacy and safety of automated US-based needle guidance with the gold standard of fluoroscopic facet joint injection, where X-ray confirmation of accurate placement will be required.

7 Conclusion

The aim of this work was to introduce, for the first time, a fully image-based visual servoing framework for neurosurgical navigation and needle guidance. Altogether, the conducted phantom experiments including a lumbar spine model have proven the stable tracking capabilities of the system without drift over time, and a reliable, clinically sufficient needle insertion accuracy in a real neurosurgical operating theater. Human volunteer experiments have furthermore underlined the applicability of the approach to clinical routine. While the visual servoing methodology is generic and can potentially be translated to other applications, immediate next steps include initial clinical trials to demonstrate the efficacy of facet joint injections using robotic ultrasound guidance for chronic spinal pain management. In the long term, we hope that this work would lead to an increased effectiveness of neurosurgigal navigation with reduced exposure to radiation compared to today's practice.

Acknowledgements and Disclosures

We thank ImFusion GmbH, Munich, Germany, for providing their image processing framework and their continuous support, and the department of nuclear medicine at Klinikum Rechts der Isar for several CT acquisitions. Furthermore, we wish to thank Julia Rackerseder for the production of the used phantoms, and Rüdiger Göbl for his assistance during experiments.
Funding: This work was partially funded by the Bayerische Forschungsstiftung award number AZ-1072-13 (project RoBildOR).
Conflict of Interest: The authors declare that they have no conflict of interest.
Compliance with Ethical Standards: Informed consent was obtained from all individual participants included in the volunteer study. All procedures performed in studies involving human participants were in accordance with the ethical standards of the institutional and national research committees.

References

1. P. Center and L. Manchikanti, "A systematic review and best evidence synthesis of effectiveness of therapeutic facet joint interventions in managing chronic spinal pain," *Pain physician*, vol. 18, pp. E535–E582, 2015.
2. S. H. Yoon, S. L. OBrien, and M. Tran, "Ultrasound guided spine injections: advancement over fluoroscopic guidance?" *Current Physical Medicine and Rehabilitation Reports*, vol. 1, no. 2, pp. 104–113, 2013.
3. I. B. Atci, N. Ucler, O. Ayden, S. Albayrak, H. Bitlisli, S. Kilic, and H. B. Altinsoy, "The comparison of pain management efficiency of ultrasonography-guided facet joint injection with fluoroscopy-guided injection in lower lumbar facet syndrome." *Neurosurgery Quarterly*, vol. 23, no. 3, pp. 246–250, 2016.
4. V. Freire, D. Grabs, M. Lepage-Saucier, and T. P. Moser, "Ultrasound-guided cervical facet joint injections a viable substitution for fluoroscopy-guided injections?" *Journal of Ultrasound in Medicine*, vol. 35, no. 6, pp. 1253–1258, 2016.
5. N. J. Soni, R. Franco-Sadud, D. Schnobrich, R. Dancel, D. M. Tierney, G. Salame, M. I. Restrepo, and P. McHardy, "Ultrasound guidance for lumbar puncture," *Neurology: Clinical Practice*, vol. 6, no. 4, pp. 358–368, 2016.
6. G. R. de Oliveira Filho, "The construction of learning curves for basic skills in anesthetic procedures: an application for the cumulative sum method," *Anesthesia & Analgesia*, vol. 95, no. 2, pp. 411–416, 2002.
7. E. Moult, T. Ungi, M. Welch, J. Lu, R. C. McGraw, and G. Fichtinger, "Ultrasound-guided facet joint injection training using perk tutor," *International journal of computer assisted radiology and surgery*, vol. 8, no. 5, pp. 831–836, 2013.
8. K. Evans, S. Roll, and J. Baker, "Work-related musculoskeletal disorders (WRMSD) among registered diagnostic medical sonographers and vascular technologists: a representative sample," *Journal of Diagnostic Medical Sonography*, 2009.
9. N. Lonjon, E. Chan-Seng, V. Costalat, B. Bonnafoux, M. Vassal, and J. Boetto, "Robot-assisted spine surgery: feasibility study through a prospective case-matched analysis," *European Spine Journal*, vol. 25, no. 3, pp. 947–955, 2016.
10. O. Zettinig, B. Fuerst, R. Kojcev, M. Esposito, M. Salehi, W. Wein, J. Rackerseder, E. Sinibaldi, B. Frisch, and N. Navab, "Toward real-time 3D ultrasound registration-based visual servoing for interventional navigation," in *2016 IEEE International Conference on Robotics and Automation (ICRA)*. IEEE, 2016, pp. 945–950.
11. D. Tran, A. A. Kamani, E. Al-Attas, V. A. Lessoway, S. Massey, and R. N. Rohling, "Single-operator real-time ultrasound-guidance to aim and insert a lumbar epidural needle," *Canadian Journal of Anesthesia/Journal canadien d'anesthésie*, vol. 57, no. 4, pp. 313–321, 2010.
12. M. Brudfors, A. Seitel, A. Rasoulian, A. Lasso, V. A. Lessoway, J. Osborn, A. Maki, R. N. Rohling, and P. Abolmaesumi, "Towards real-time, tracker-less 3D ultrasound guidance for spine anaesthesia," *International Journal of Computer Assisted Radiology and Surgery*, pp. 1–11, 2015.
13. C. X. Yan, B. Goulet, J. Pelletier, S. J.-S. Chen, D. Tampieri, and D. L. Collins, "Towards accurate, robust and practical ultrasound-CT registration of vertebrae for image-guided spine surgery," *International Journal of Computer Assisted Radiology and Surgery*, vol. 6, no. 4, pp. 523–537, 2011.
14. T. Ungi, P. Abolmaesumi, R. Jalal, M. Welch, I. Ayukawa, S. Nagpal, A. Lasso, M. Jaeger, D. P. Borschneck, G. Fichtinger, and P. Mousavi, "Spinal needle navigation by tracked ultrasound snapshots," *Biomedical Engineering, IEEE Transactions on*, vol. 59, no. 10, pp. 2766–2772, 2012.
15. A. Rasoulian, J. Osborn, S. Sojoudi, S. Nouranian, V. A. Lessoway, R. N. Rohling, and P. Abolmaesumi, "A system for ultrasound-guided spinal injections: A feasibility study," in *Information Processing in Computer-Assisted Interventions*. Springer, 2014, pp. 90–99.
16. P. Abolmaesumi, S. Salcudean, and W. Zhu, "Visual servoing for robot-assisted diagnostic ultrasound," in *Engineering in Medicine and Biology Society, 2000. Proceedings of the 22nd Annual International Conference of the IEEE*, vol. 4. IEEE, 2000, pp. 2532–2535.
17. R. Nakadate, J. Solis, A. Takanishi, E. Minagawa, M. Sugawara, and K. Niki, "Out-of-plane visual servoing method for tracking the carotid artery with a robot-assisted ultrasound diagnostic system," in *Robotics and Automation (ICRA), 2011 IEEE International Conference on*. IEEE, 2011, pp. 5267–5272.

18. C. Nadeau and A. Krupa, "Intensity-based ultrasound visual servoing: Modeling and validation with 2-d and 3-d probes," *Robotics, IEEE Transactions on*, vol. 29, no. 4, pp. 1003–1015, 2013.
19. A. Krupa, D. Folio, C. Novales, P. Vieyres, and T. Li, "Robotized tele-echography: an assisting visibility tool to support expert diagnostic," *Systems Journal, IEEE*, no. 99, pp. 1 – 10, 2014.
20. P. Chatelain, A. Krupa, and N. Navab, "Optimization of ultrasound image quality via visual servoing," in *IEEE Int. Conf. on Robotics and Automation, ICRA 2015*.
21. S. Virga, O. Zettinig, M. Esposito, K. Pfister, B. Frisch, T. Neff, N. Navab, and C. Hennersperger, "Automatic force-compliant robotic ultrasound screening of abdominal aortic aneurysms," in *Intelligent Robots and Systems (IROS), 2016 IEEE/RSJ International Conference on*, vol. in press, October 2016.
22. T. K. Adebar, A. E. Fletcher, and A. M. Okamura, "3-D Ultrasound-Guided Robotic Needle Steering in Biological Tissue," *Biomedical Engineering, IEEE Transactions on*, vol. 61, no. 12, pp. 2899–2910, 2014.
23. A. Krupa, "3D steering of a flexible needle by visual servoing," in *Medical Image Computing and Computer-Assisted Intervention–MICCAI 2014*. Springer, 2014, pp. 480–487.
24. C. Nadeau, H. Ren, A. Krupa, and P. Dupont, "Intensity-based visual servoing for instrument and tissue tracking in 3D ultrasound volumes," *Automation Science and Engineering, IEEE Transactions on*, vol. 12, no. 1, pp. 367–371, 2015.
25. J. De Schutter and H. Van Brussel, "Compliant robot motion ii. a control approach based on external control loops," *The International Journal of Robotics Research*, vol. 7, no. 4, pp. 18–33, 1988.
26. A. Karamalis, W. Wein, O. Kutter, and N. Navab, "Fast hybrid freehand ultrasound volume reconstruction," in *SPIE Medical Imaging*. International Society for Optics and Photonics, 2009, pp. 726 114–726 114.
27. W. Wein and A. Khamene, "Image-based method for in-vivo freehand ultrasound calibration," in *Medical Imaging*. International Society for Optics and Photonics, 2008, pp. 69 200K–69 200K.
28. B. Fuerst, W. Wein, M. Müller, and N. Navab, "Automatic ultrasound–MRI registration for neurosurgery using the 2D and 3D LC2 metric," *Medical Image Analysis*, vol. 18, no. 8, pp. 1312–1319, 2014.
29. M. Modat, G. R. Ridgway, Z. A. Taylor, M. Lehmann, J. Barnes, D. J. Hawkes, N. C. Fox, and S. Ourselin, "Fast free-form deformation using graphics processing units," *Computer methods and programs in biomedicine*, vol. 98, no. 3, pp. 278–284, 2010.
30. M. J. Powell, "The BOBYQA algorithm for bound constrained optimization without derivatives," *Cambridge NA Report NA2009/06, University of Cambridge, Cambridge*, 2009.
31. W. Wein, S. Brunke, A. Khamene, M. R. Callstrom, and N. Navab, "Automatic CT-ultrasound registration for diagnostic imaging and image-guided intervention," *Medical Image analysis*, vol. 12, no. 5, pp. 577–585, 2008.
32. A. Lasso, T. Heffter, A. Rankin, C. Pinter, T. Ungi, and G. Fichtinger, "PLUS: Open-source toolkit for ultrasound-guided intervention systems," *IEEE Transactions on Biomedical Engineering*, no. 10, pp. 2527–2537, Oct 2014.
33. J. Tokuda, G. S. Fischer, X. Papademetris, Z. Yaniv, L. Ibanez, P. Cheng, H. Liu, J. Blevins, J. Arata, A. J. Golby, T. Kapur, S. Pieper, E. C. Burdette, G. Fichtinger, C. M. Tempany, and N. Hata, "OpenIGTLink: an open network protocol for image-guided therapy environment," *The International Journal of Medical Robotics and Computer Assisted Surgery*, vol. 5, no. 4, pp. 423–434, 2009.
34. R. Y. Tsai and R. K. Lenz, "A new technique for fully autonomous and efficient 3d robotics hand/eye calibration," *IEEE Transactions on Robotics and Automation*, vol. 5, no. 3, pp. 345–358, 1989.
35. Y. Liu, C. Zeng, M. Fan, L. Hu, C. Ma, and W. Tian, "Assessment of respiration-induced vertebral motion in prone-positioned patients during general anaesthesia," *The International Journal of Medical Robotics and Computer Assisted Surgery*, vol. 12, no. 2, pp. 214–218, 2016.
36. K. Galiano, A. A. Obwegeser, G. Bodner, M. Freund, H. Maurer, F. S. Kamelger, R. Schatzer, and F. Ploner, "Ultrasound guidance for facet joint injections in the lumbar spine: a computed tomography-controlled feasibility study," *Anesthesia & Analgesia*, vol. 101, no. 2, pp. 579–583, 2005.
37. R. E. Kalman, "A new approach to linear filtering and prediction problems," *Journal of basic Engineering*, vol. 82, no. 1, pp. 35–45, 1960.

38. B.-H. Jung, B.-H. Kim, and S.-M. Hong, "Respiratory motion prediction with extended kalman filters based on local circular motion model," *International Journal of Bio-Science and Bio-Technology*, vol. 5, no. 1, pp. 51–58, 2013.
39. J. Provost, C. Papadacci, J. E. Arango, M. Imbault, M. Fink, J.-L. Gennisson, M. Tanter, and M. Pernot, "3D ultrafast ultrasound imaging in vivo," *Physics in Medicine and biology*, vol. 59, no. 19, p. L1, 2014.